Bioactive Materials 6 (2021) 4389–4401

Contents lists available at ScienceDirect

Bioactive Materials

journal homepage: www.sciencedirect.com/journal/bioactive-materials

Copper single-atom catalysts with photothermal performance and enhanced nanozyme activity for bacteria-infected wound therapy

Xianwen Wang [a,1], Qianqian Shi [b,1], Zhengbao Zha [b,**], Dongdong Zhu [b], Lirong Zheng [d], Luoxiang Shi [c], Xianwen Wei [c], Lian Lian [e], Konglin Wu [c,***], Liang Cheng [a,*]

[a] Institute of Functional Nano & Soft Materials (FUNSOM), Jiangsu Key Laboratory for Carbon-based Functional Materials and Devices, Soochow University, Suzhou, 215123, PR China
[b] School of Food and Biological Engineering, Hefei University of Technology, Hefei, 230009, PR China
[c] Institute of Clean Energy and Advanced Nanocatalysis, School of Chemistry and Chemical Engineering, Anhui University of Technology, Maanshan, 243002, PR China
[d] Beijing Synchrotron Radiation Facility (NSRF), Institute of High Energy Physics, Chinese Academy of Science, Beijing, 100049, China
[e] Department of Oncology, Suzhou Xiangcheng People's Hospital, Suzhou, 215131, China

ARTICLE INFO

Keywords:
Copper single-atom catalysts
Nanozymes
Photothermal therapy
Antibacterial
Catalytic therapy

ABSTRACT

Nanozymes have become a new generation of antibiotics with exciting broad-spectrum antibacterial properties and negligible biological toxicity. However, their inherent low catalytic activity limits their antibacterial properties. Herein, Cu single-atom sites/N doped porous carbon (Cu SASs/NPC) is successfully constructed for photothermal-catalytic antibacterial treatment by a pyrolysis-etching-adsorption-pyrolysis (PEAP) strategy. Cu SASs/NPC have stronger peroxidase-like catalytic activity, glutathione (GSH)-depleting function, and photothermal property compared with non-Cu-doped NPC, indicating that Cu doping significantly improves the catalytic performance of nanozymes. Cu SASs/NPC can effectively induce peroxidase-like activity in the presence of H_2O_2, thereby generating a large amount of hydroxyl radicals (•OH), which have a certain killing effect on bacteria and make bacteria more susceptible to temperature. The introduction of near-infrared (NIR) light can generate hyperthermia to fight bacteria, and enhance the peroxidase-like catalytic activity, thereby generating additional •OH to destroy bacteria. Interestingly, Cu SASs/NPC can act as GSH peroxidase (GSH-Px)-like nanozymes, which can deplete GSH in bacteria, thereby significantly improving the sterilization effect. PTT-catalytic synergistic antibacterial strategy produces almost 100% antibacterial efficiency against *Escherichia coli* (*E. coli*) and methicillin-resistant *Staphylococcus aureus* (*MRSA*). *In vivo* experiments show a better PTT-catalytic synergistic therapeutic performance on MRSA-infected mouse wounds. Overall, our work highlights the wide antibacterial and anti-infective bio-applications of Cu single-atom-containing catalysts.

1. Introduction

Pathogenic bacteria are the main cause of bacterial infectious diseases, which seriously threaten human health [1]. At present, treatment is heavily dependent on antibiotics, leading to a rapid increase in multi-drug resistance and a sharp decline in therapeutic effects [2–4]. In recent years, emerging nanozymes have become a new generation of antibiotics due to their broad-spectrum antibacterial activity, low toxicity, and no drug resistance [5,6]. Generally, nanozymes with peroxidase-like activity specifically catalyze the conversion of hydrogen peroxide (H_2O_2) into highly toxic reactive oxygen species (ROS), such as hydroxyl radicals (•OH), to attack the bacterial membranes of weakly acidic infection sites [7,8]. Previous studies have shown that ROS is an important factor for the immune system to perform antibacterial effects, where ROS can kill bacteria by destroying their cell membranes, DNA, proteins, etc. [9,10] Compared with antibiotics, the ROS-based sterilization method can avoid the occurrence of bacterial resistance, therefore, the development of ROS-based antibacterial strategies is very

Peer review under responsibility of KeAi Communications Co., Ltd.
* Corresponding author.
** Corresponding author.
*** Corresponding author.
E-mail addresses: zbzha@hfut.edu.cn (Z. Zha), klwuchem@ahut.edu.cn (K. Wu), lcheng2@suda.edu.cn (L. Cheng).
[1] These authors contribute equally to this work.

https://doi.org/10.1016/j.bioactmat.2021.04.024
Received 9 March 2021; Received in revised form 12 April 2021; Accepted 14 April 2021

effective and promising [11]. At present, it has been proved that many nanomaterials with enzyme-like and antibacterial properties, including noble metal nanoparticles [12], carbon-based nanomaterials [13], metal oxides [11,14], and metal chalcogenides [15–17], can eradicate different types of bacteria, even drug-resistant bacteria. Unfortunately, the low catalytic activity of nanozymes greatly limits their antibacterial effects [18]. In addition, it is also worth noting that the microenvironments of the infection sites usually have abnormally high expression of glutathione (GSH) levels, which are caused by anaerobic glycolysis, greatly reducing the catalytic therapeutic effects of nanozymes [19–21]. Thus, there is still a great need for antibacterial nanozymes with enhanced catalytic activity and GSH-depleting function.

Based on the Arrhenius equation, the rate of chemical reactions is positively related to temperature [22]. Starting from the basic principle

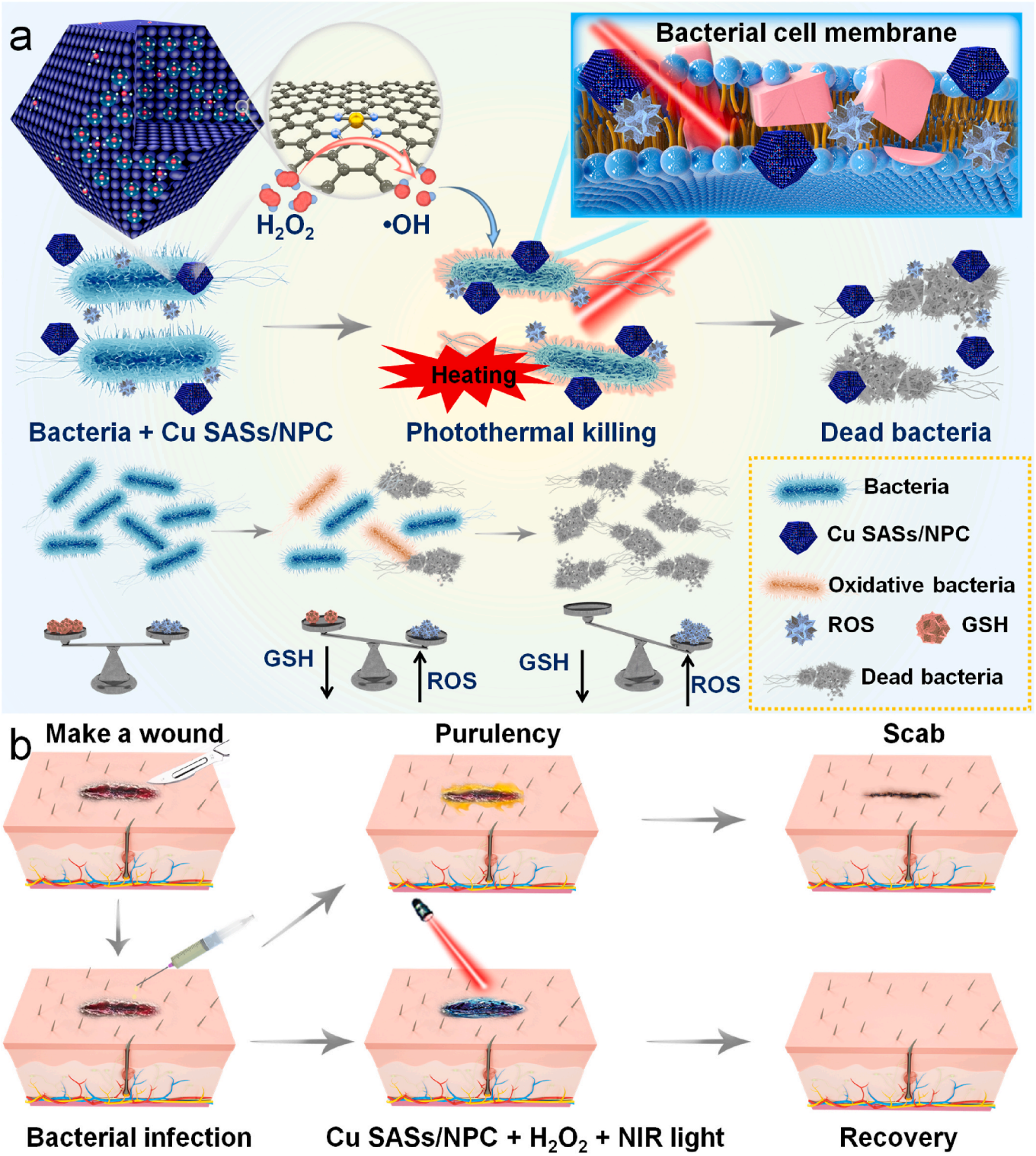

Scheme 1. Cu SASs/NPC with GSH-depleting performance were successfully synthesized for photothermal-catalytic therapy against bacterial. Cu SASs/NPC as GSH-like mimetic enzyme and HRP-like nanozyme for eradicating *E. coli* and *MRSA in vitro*, (b) and for the treatment of *MRSA* infection *in vivo*.

that raising temperature can accelerate the rate of chemical reactions, increasing temperature of the bacterial infection sites to enhance the catalytic rate of nanozymes is an effective strategy [16]. Therefore, high temperature can significantly promote the production of ROS, thereby effectively killing bacteria. However, it is impractical to heat nanozymes by direct contact with external heat sources, especially for *in vivo* antibacterial applications [23]. To overcome these shortcomings, the combination of nanozyme-based catalytic therapy and photothermal therapy (PTT) is a promising approach [24,25]. PTT is an effective method that uses photothermal reagents to generate local high temperature to treat bacterial infections under near-infrared (NIR) light irradiation [26,27]. Although PTT has the advantages of high controllability and minimal invasiveness, relatively high-power laser intensity can still cause side effects on healthy tissues [14]. Therefore, the combination of catalytic therapy and PTT can simultaneously enhance the catalytic production of ROS while reducing the collateral damage of PTT [15,27]. Although several nanozymes have been reported for PTT-catalytic antibacterial treatment, the treatment performance of these nanozymes is still limited [12,14–16,18]. Among the numerous nanozymes, copper-based nanomaterials not only have strong photothermal performance, but also undergo Fenton-like reactions in a wide pH range, thus exhibiting effects similar to iron-based catalysts [28]. Cu^{+} can effectively catalyze H_2O_2 to produce •OH, and its catalytic efficiency rate (1×10^4 $M^{-1}s^{-1}$) is much higher than that of Fe^{2+} (76 $M^{-1}s^{-1}$) [29–31]. In addition, copper-based nanomaterials also exhibit the function of GSH depletion, thereby improving the therapeutic effect of ROS-related therapies [32]. Based on this, it is extremely important to develop copper-based nanozymes with high catalytic performance and GSH-depleting function for PTT-catalytic antibacterial therapy.

Thanks to recent great achievements in the field of catalysis, single-atom catalysts (SACs), in which isolated metal atoms are located on the carrier, have been used in catalysis due to their high catalytic properties

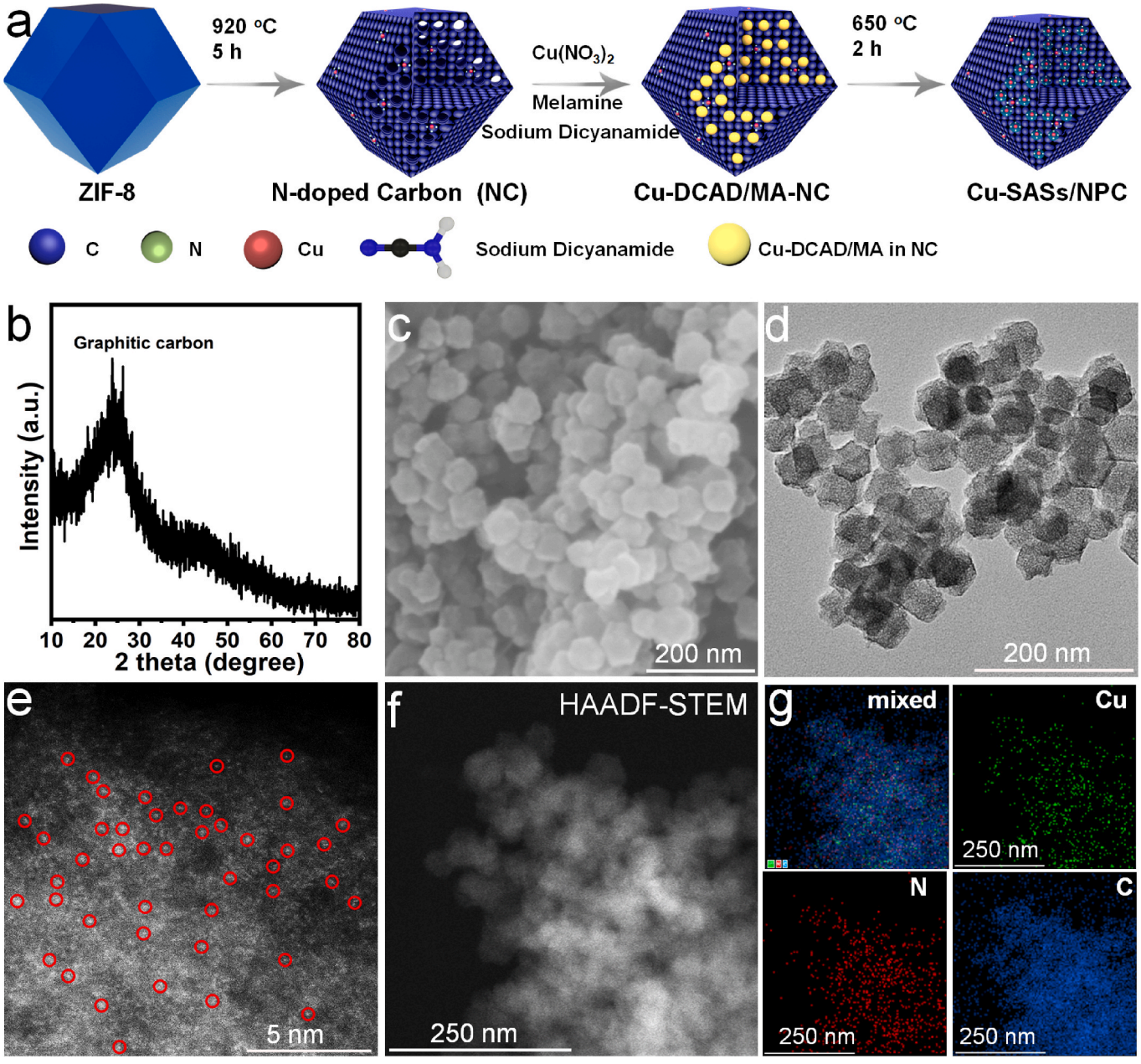

Fig. 1. Synthetic process and characterization of Cu SASs/NPC. (a) Schematic illustration synthesis of Cu SASs/NPC by a PEAP strategy. (b) XRD pattern; (c) SEM image; (d) TEM image; (e) AC-HAADF-STEM image; and (f) HAADF-STEM image and corresponding (g) EDS mapping images of Cu SASs/NPC.

[33–36]. SACs have strong catalytic activity and can maximize metal utilization, which is especially important for cancer/antibacterial treatments to achieve effective disease treatment with relatively low metal concentrations [37–39]. Due to its good catalytic effect, excellent biosafety, special mesoporous structure, and large specific surface area, N-doped porous carbon (NPC) has been widely used as special nanoplatforms for the construction of SACs. Herein, Cu single-atom sites/NPC (Cu SASs/NPC) fabricated by a pyrolysis-etching-adsorption-pyrolysis (PEAP) strategy can act as nanozymes for photothermal-catalytic antibacterial therapy (Scheme 1). Cu SASs/NPC has stronger catalytic activity, GSH-depleting performance, and photothermal effect compared to NPC without Cu doping. The as-prepared Cu SASs/NPC can use as peroxidase-like nanozymes to efficiently catalyze H_2O_2 to produce hydroxyl radicals (•OH), thereby causing obvious killing of bacteria. The photothermal effect of Cu SASs/NPC under laser irradiation can further improve the peroxidase-like catalytic effect, thereby generating more ROS and achieving *in vitro* better antibacterial effects. More importantly, Cu SASs/NPC effectively eradicates internal bacterial infections propagated at wounds by MRSA pathogens, thereby obtaining *in vivo* better wound healing. Overall, our work highlights the good antibacterial properties of Cu single-atom-containing catalysts and further expands its application in biomedicine.

2. Results and discussion

Cu SASs/NPC antibacterial materials were prepared by a PEAP strategy (Fig. 1a). Firstly, NPC was obtained by pyrolysis of ZIF-8 precursors at 920 °C for 5 h in a tubular furnace, and then was further treated with 3 M HCl. As shown in Figs. S1a and S2, the morphology of NPC remained the same as that of the ZIF-8 precursors. The XRD result showed that there was no zinc or oxide in the NPC (Fig. S1b), and the peak at about 25° belonged to the graphitized carbon [40,41]. Subsequently, the Cu^{2+}-sodium dicyandiamide/melamine-NPC (Cu^{2+}-DCDA/MA-NPC) was prepared by using NPC to adsorb Cu ions, sodium dicyandiamide, and melamine in a mixed solvent with isopropanol and water. Finally, the Cu SASs/NPC was prepared by pyrolysis of Cu^{2+}-DCDA/MA-NPC at 650 °C for 2 h in a tubular furnace. Fig. 1b displayed the XRD pattern of Cu SASs/NPC, no peaks of Cu or its oxides were found, indicating that Cu might exist in the form of atomic dispersion in the NPC matrix. Compared with NPC, the morphology of Cu SASs/NPC had no obvious change (Fig. 1c). The hydrodynamic size of Cu SASs/NPC was 193 ± 19 nm and the PDI value was ~0.32,

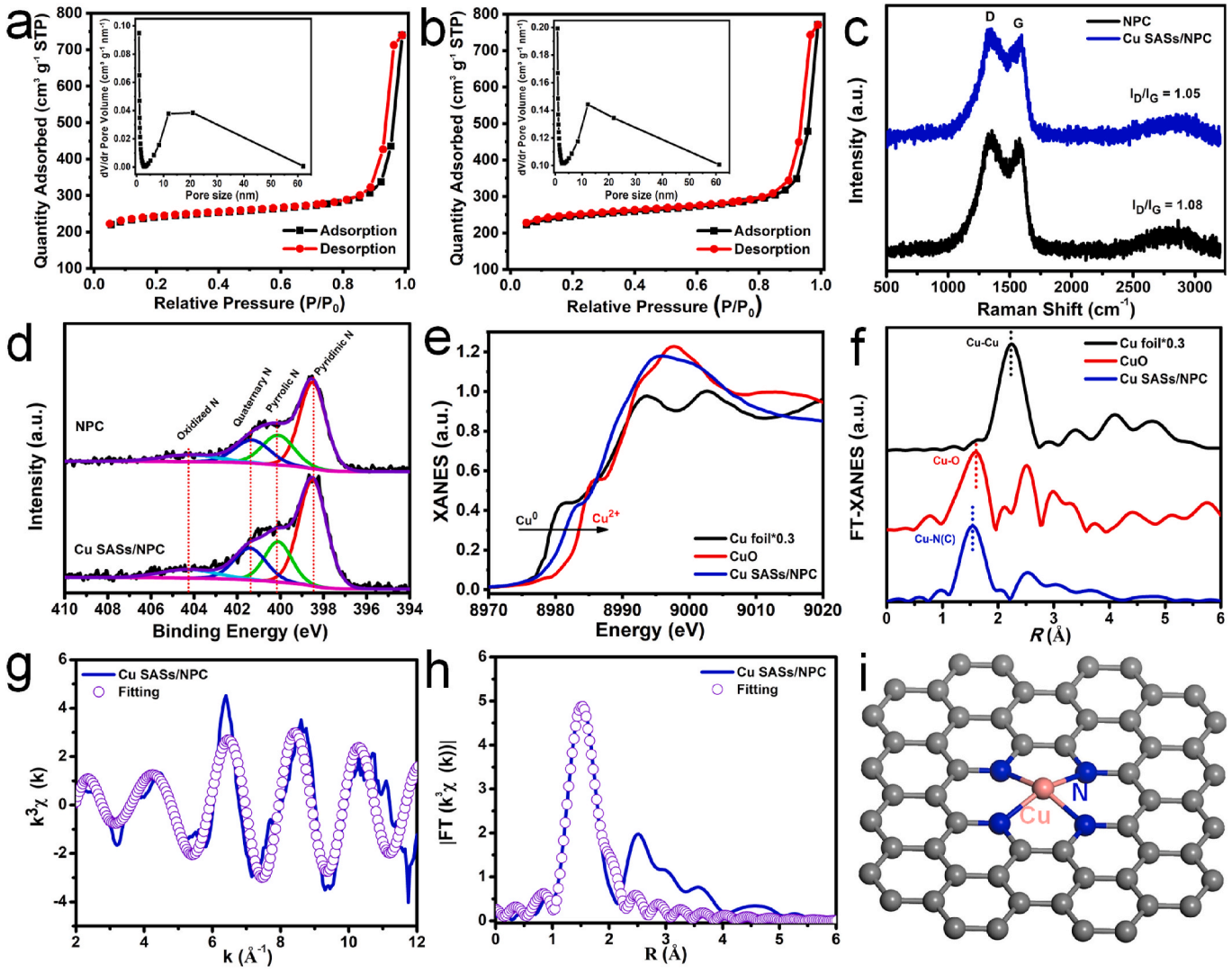

Fig. 2. Structure characterization of Cu SASs/NPC and NPC. N_2 absorption and desorption curves and pore size distributions for (a) NPC and (b) Cu SASs/NPC. (c) Raman spectra of NPC (black curve) and Cu SASs/NPC (blue curve). (d) N 1s spectra of NPC and Cu SASs/NPC. (e) XANES spectrum of Cu SASs/NPC and reference samples. (f) Fourier transform (FT) *k* [3]-weighted Cu K-edge EXAFS oscillation spectra of Cu SASs/NPC and reference samples. (g) EXAFS fitting result of Cu SASs/NPC at k space. (h) EXAFS fitting result of Cu SASs/NPC in R space. (i) Schematic model of atomic level structure for Cu SASs/NPC.

indicating the relatively good solution dispersion of the synthesized Cu SASs/NPC (Fig. S3). TEM image further showed that there were no obvious clusters or particles in the Cu SASs/NPC (Fig. 1d). In addition, TEM result also exhibited that the product had an abundant pore structure. Aberration-corrected high-angle annular dark-field scanning transmission electron microscopy (AC-HAADF-STEM) image indicated that there were no clusters and particles in the Cu SASs/NPC (Fig. 1e), further confirmed by XRD and TEM results. According to the difference of the atomic number of elements, the bright white spots in the NPC matrix could attribute to the atomically dispersed Cu (marked with red circles) [42,43]. Further HAADF-STEM (Fig. 1f) and the corresponding EDS mapping (Fig. 1g) results showed that Cu, N, and C were uniformly distributed in the samples. In order to obtain the content of Cu in the Cu SASs/NPC antibacterial materials, the product was characterized by inductively coupled plasma optical emission spectrometry (ICP-OES). The mass percent of Cu in Cu SASs/NPC was ~1.15%, which indicated that the PEAP method was an extremely effective strategy to obtain Cu SASs (Table S1).

The N_2 adsorption/desorption experiments under 77 K were used to characterize the specific surface areas and pore size distribution of NPC and Cu SASs/NPC, and the relevant data were listed in Table S2. The NPC and Cu SASs/NPC displayed similar adsorption/desorption characteristics (Fig. 2a–b), indicating that the structure was not damaged during the second heat treatment. The Brunauer-Emmett-Teller (BET) specific surface areas of NPC and Cu SASs/NPC were 748.8 and 767.8 $m^2\ g^{-1}$, respectively. Based on the Barrett-Joyner-Halenda (BJH) method, the cumulative pore volume and average pore size were ~0.84 $cm^3\ g^{-1}$ and 10.3 nm for NPC, and 0.88 $cm^3\ g^{-1}$ and 10.0 nm for Cu SASs/NPC. Raman spectra of NPC and Cu SASs/NPC displayed the two typical peaks at about 1390 cm^{-1} for D band (defects in the carbon structure) and 1530 cm^{-1} for G band (sp^2-hybridized carbon structure unit) in graphitized carbon (Fig. 2c) [44,45]. As shown in Fig. 2c and Table S3, the D band in Cu SASs/NPC (1400.6 cm^{-1}) was shifted to the higher wavenumber than that of the NPC (1388.2 cm^{-1}), but the G band in Cu SASs/NPC (1531 cm^{-1}) was shifted to the lower wavenumber than that of NPC (1532.1 cm^{-1}). Based on the Raman spectra (Fig. 2c and Table S3), the I_D/I_G values of NPC and Cu SASs/NPC were 1.08 and 1.05, respectively, which indicated that the Cu SASs/NPC appeared less defective than that of NPC due to the introduction of Cu SASs and N into the carbon skeleton [37,46]. The N 1s XPS spectra of Cu SASs/NPC showed that four types N of pyridinic N (398.5 eV), pyrrolic N (400.1 eV), graphitic N (401.4 eV), and weak oxidized N (404.3 eV) species, respectively (Fig. 2d and Table S4). Furthermore, the percentage of pyridinic N in Cu SASs/NPC was higher than that of NPC due to the combination of pyridinic N and Cu SASs [37]. Synchrotron radiation is an effective method to reveal the fine structure of SASs. Here, the X-ray absorption near-edge structure (XANES) spectroscopy and extended X-ray absorption fine structure (EXAFS) spectroscopy were applied to reveal the electronic structure and coordination environment of Cu in the Cu SASs/NPC. From the Cu K-edges XANES (Fig. 2e) spectra showed that the Cu K-edge profile of Cu SASs/NPC was between the Cu foil and CuO, which indicated that there was a part of the positive charge for Cu SASs in the Cu SASs/NPC, and its oxidation state was between 0 and + 2. Fourier transform (FT) EXAFS (FT-EXAFS) spectra with k^3-weighted of Cu K-edges for Cu SASs/NPC (Fig. 2f, blue curve), CuO (red curve), and Cu foil*0.3 (black curve) were also obtained. As shown in Fig. 2f (blue curve), the FT-EXAFS spectrum of Cu SASs/NPC displayed the main peak at about 1.53 Å, which was attributed to the Cu–N(C) coordination. There was no scattering of Cu–Cu coordination signal. These results indicated that Cu existed in the form of atomically dispersed on NPC. Further fitting results of synchrotron radiation data showed that the first shell coordination number at 1.90 Å for Cu–N(C) was 4.2 (Fig. 2g–h, and Table S4), indicating that the porphyrin-like Cu–N_4 structural units (Fig. 2i) were formed by the combination of one Cu and four N atoms in the Cu SASs/NPC. Therefore, Cu SASs/NPC with porphyrin-like Cu–N_4 structural units was successfully synthesized by a PEAP strategy.

SACs have received increasing attention in various catalysis fields in recent years [47]. The emerging nano-catalytic drugs also provide a new strategy for antibacterial therapy without the use of toxic chemicals. The unique properties of SACs also make them promising candidates for antibacterial therapy [33]. First, the peroxidase-like catalytic activity of Cu SASs/NPC was evaluated using H_2O_2 and o-phenylenediamine (OPDA)/3, 3′,5, 5′-tetramethylbenzidine (TMB) as the substrates (Fig. 3a). OPDA and TMB are indicators of •OH, the production of which can change its color from colorless to yellow or blue [48]. The groups of H_2O_2 + TMB and Cu SASs/NPC + H_2O_2 alone did not produce blue color or absorption at 654 nm. While the group of Cu SASs/NPC + TMB led to a weak absorption at 654 nm in the UV–vis–NIR spectra, which showed that the low oxidase-like activity could be ignored. Compared with other groups, the group of Cu SASs/NPC + TMB + H_2O_2 displayed the strongest absorption peak at 654 nm, indicating that Cu SASs/NPC had strong peroxidase-like catalytic activity (Fig. S4). When Cu SASs/NPC reacted with different concentrations of H_2O_2, as the concentration of H_2O_2 increased, the •OH produced by the system significantly enhanced, showing that the peroxidase-like catalytic performance of Cu SASs/NPC depended the concentration of H_2O_2 (Fig. 3b). In addition, the peroxidase-like catalytic performance of Cu SASs/NPC was further tested with OPDA (Fig. 3c and Fig. S5) and methylene blue (MB) probes (Fig. 3d and Figs. S6–7). Similar phenomena were found using OPDA and MB probes, which fully proved that Cu SASs/NPC had excellent peroxidase-like catalytic effect. However, the NPC without Cu doping only showed weak peroxidase-like catalytic activity (Fig. S8).

A large number of •OH produced by peroxidase-like nanozymes can be depleted by GSH, and the concentration increases significantly at the infection sites due to the abnormal encapsulation of extracellular polymeric substances [19]. Copper-based catalysts usually have good GSH depletion capabilities due to their multivalent properties [32]. Therefore, we speculated that Cu SASs/NPC may have excellent GSH depletion capabilities. The GSH-depleting function of Cu SASs/NPC was evaluated using 5, 5′-dithio-bis (2-nitrobenzoic acid) (DTNB) probe. It could be found that the characteristic peak of DTNB at 420 nm was significantly reduced under the condition of Cu SASs/NPC. After reaction for 15 min, the characteristic peak of DTNB was basically no longer visible, indicating that Cu SASs/NPC could efficiently consume almost all GSH (Fig. 3e). Even when the concentration of Cu SASs/NPC was as low as ~50 μg/mL, GSH also was completely consumed after 6 h (Fig. 3f). The higher concentration of Cu SASs/NPC, the faster GSH was consumed in the system, indicating the concentration-dependent manner of GSH consumption by Cu SASs/NPC (Fig. 3g and Fig. S9). Even when the content of GSH was much higher than that of Cu SASs/NPC, the GSH could still be completely consumed. Therefore, the ability of Cu SASs/NPC to consume GSH did not come from redox. This might be due to the fact that Cu SASs/NPC acted as a GSH peroxidase (GSH-Px)-like mimetic enzyme, which could efficiently deplete GSH at a lower concentration, resulting in satisfactory GSH-depleting ability. In addition, Cu SASs/NPC had better GSH-depleted performance than NPC (Fig. S10).

Satisfactory NIR absorption is the most basic condition for photothermal reagents. It could be seen from that Cu SASs/NPC possessed strong NIR absorption, and the absorption intensity was positively correlated with the material concentration (Fig. 3h), which implied that Cu SASs/NPC was good photothermal agents. Interestingly, the absorption of Cu SASs/NPC in the NIR region was significantly stronger than that of NPC without Cu doping (Fig. S11). In addition, the mass extinction coefficient of Cu SASs/NPC was calculated to be ~2.246 L/g/cm (Fig. S12). In order to study their photothermal performance, the heating effect of different concentrations of Cu SASs/NPC under 808 nm laser irradiation (1.0 W/cm^2, 10 min) was studied. It found that Cu SASs/NPC had more prominent photothermal effects than that of NPC under the same laser irradiation condition (Figs. S13–14). The thermal images and photothermal heating curves of Cu SASs/NPC under 808 nm laser irradiation showed that Cu SASs/NPC had concentration and

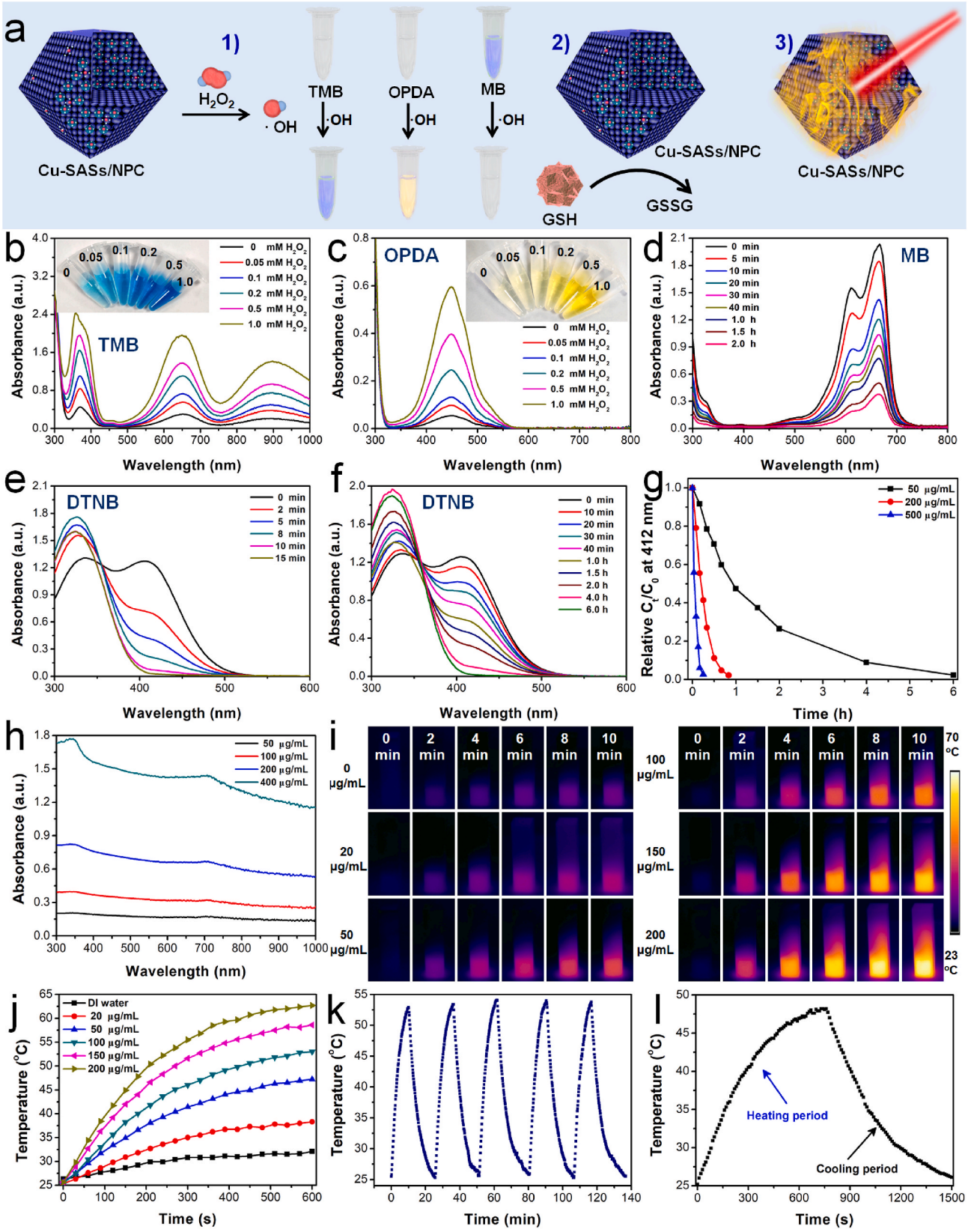

Fig. 3. HRP-like catalytic performance, GSH-depleting function, and photothermal effect of Cu SASs/NPC. (a)Properties of Cu SASs/NPC: 1) catalytic effect; 2) GSH-depleted function; 3) photothermal performance. HRP-like catalytic performance of Cu SASs/NPC in the presence of various concentrations of H_2O_2 using different probes: (b) TMB; (c) OPDA. (d) Time-dependent degradation of MB in the presence of Cu SASs/NPC and H_2O_2. Time-dependent GSH depletion in the presence of Cu SASs/NPC with different concentrations: (e) 500 μg/mL; (f) 50 μg/mL (g) GSH consumption rate of Cu SASs/NPC. (h) UV–vis–NIR spectra of Cu SASs/NPC. (i) Thermal images, (j) and temperature-elevating curves of Cu SASs/NPC with different concentrations under 808 nm laser irradiation (1.0 W/cm^2, 10 min). (k) Photothermal stability (five laser ON/OFF cycles) of Cu SASs/NPC. (l) Temperature variation of primary heating and cooling of Cu SASs/NPC.

power density depended photothermal heating performance (Fig. 3i–j, Figs. S15–16). Excellent photothermal stability is a very important thing during PTT. Therefore, the photothermal stability of Cu SASs/NPC was evaluated. After five laser ON/OFF cycles, the amplitude of temperature elevation (Fig. 3k), UV–vis–NIR spectra, and TEM image of Cu SASs/NPC did not change significantly (Fig. S17), indicating the good photothermal stability of Cu SASs/NPC. Since then, the photothermal conversion efficiency of Cu SASs/NPC was calculated to be ~82.78% (Fig. 3l and Fig. S18), much stronger than the previously reported Cu-based photothermal agents, such as Cu_2Se hollow cubes (~50.89%) [31], $Cu_{2-x}S$ nanoparticles (~30.8%) [49], Cu_3BiS_3 nanorods (~40.7%) [50]. The good photothermal conversion efficiency of Cu SASs/NPC may

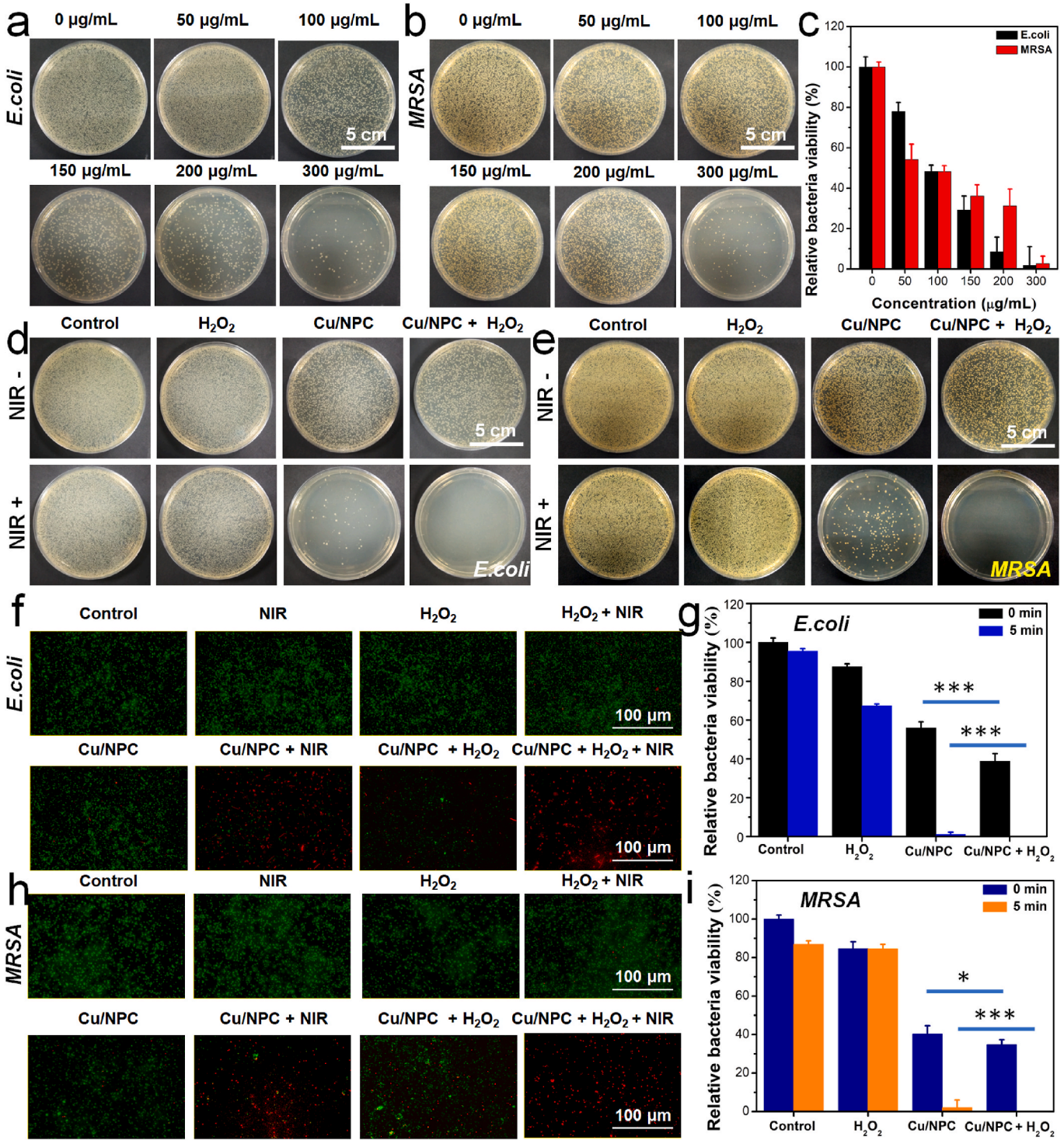

Fig. 4. *In vitro* antibacterial effect of Cu SASs/NPC. Photographs of bacterial colonies of (a) *E. coli* and (b) *MRSA* treated by Cu SASs/NPC (0, 50, 100, 150, 200, 300 μg/mL). (c) Relative bacterial viability of *E. coli* and *MRSA* after treating Cu SASs/NPC based on (a)–(b). Photographs of bacterial colonies of (d) *E. coli* and (e) *MRSA* after different treatments (control, NIR light; H_2O_2; NIR light + H_2O_2; Cu SASs/NPC; Cu SASs/NPC + H_2O_2; Cu SASs/NPC + NIR light; Cu SASs/NPC + H_2O_2 + NIR light). Relative bacterial viability of (g) *E. coli* and (i) *MRSA* after different treatments based on (d)–(e). Fluorescence staining images of (f) *E. coli* and (h) *MRSA* using SYTO9/PI after different treatments. Statistical analysis was performed using the Student's two-tailed *t*-test (***P < 0.001, **P < 0.01, and *P < 0.05).

be attributed to its good near-infrared absorption. In general, Cu SASs/NPC could act as peroxidase-like and GSH-P_x-like nanozymes had good •OH generation ability, GSH consumption function, and photothermal performance, showing good bactericidal potential.

Considering the above-mentioned excellent properties of Cu SASs/NPC, then the possibility of Cu SASs/NPC as a potential photothermal nanomaterial combined with the peroxidase-like catalytic effect of synergistically ablating bacteria was investigated. Using *Escherichia coli* (*E. coli*) and methicillin-resistant *Staphylococcus aureus* (*MRSA*) as model, the *in vitro* antibacterial performance of Cu SASs/NPC was studied. Firstly, the antibacterial effect of Cu SASs/NPC was evaluated alone. Fig. 4a–c were the photographs and the corresponding quantitative bacterial viability of bacterial colonies of *E. coli* and *MRSA* treated by Cu SASs/NPC with different concentrations. It could be found that Cu SASs/NPC had a certain degree of killing effect on both bacteria (*E. coli* and *MRSA*), and the antibacterial effect depended on the concentration of Cu SASs/NPC (Fig. 4a–b). When the concentration of Cu SASs/NPC reached ~100 μg/mL, the killing rate of the material itself to both bacteria was close to 50% (Fig. 4c). Compared with NPC, Cu SASs/NPC had more obvious antibacterial effects at the same concentration, which might be due to the doping of Cu atoms (Fig. S19). The antibacterial effect of Cu SASs/NPC might be derived from the catalytic effect of Fenton-like reaction due to the high expression of H_2O_2 in bacteria. To further study the synergistic antibacterial performance of Cu SASs/NPC, the bacteria were treated as follows: (1) control, (2) NIR light; (3) H_2O_2; (4) NIR light + H_2O_2; (5) Cu SASs/NPC; (6) Cu SASs/NPC + H_2O_2; (7) Cu SASs/NPC + NIR light; (8) Cu SASs/NPC + H_2O_2 + NIR light. As shown in Fig. 4d–e, the number of bacterial colonies in the H_2O_2 group was slightingly less than that in the control group regardless of exposure to the 808 nm NIR laser, indicating that H_2O_2 (100 μM) had the weaker antibacterial effect. As for Cu SASs/NPC group, only a small part of the colonies was decreased, attributed to the antibacterial effect of Cu SASs/NPC itself. However, the relative bacterial viability of the Cu SASs/NPC + H_2O_2 group against *MRSA* and *E. coli* decreased to ~34.8% and ~38.82%, respectively, indicating that Cu SASs/NPC could catalyze the decomposition of H_2O_2 to generate toxic •OH to kill bacteria. Although the Cu SASs/NPC + H_2O_2 group could destroy most of the bacteria, it cannot achieve the required antibacterial effect against bacterial infections. Combining the high photothermal effect and peroxidase-like catalytic activity of Cu SASs/NPC, the antibacterial effect remarkedly improved and the survival rate of the Cu SASs/NPC + H_2O_2 + NIR light group against *E. coli* and *MRSA* reached 0%. In contrast, the survival rates of the Cu SASs/NPC + NIR group against *E. coli* and *MRSA* were only ~1.01% and ~2.1%, respectively (Fig. 4g, i). Meanwhile, the bactericidal effect was directly observed by conducting dead/live staining (PI and Syto9) of bacteria after different treatments (Fig. 4f, h), and the results were consistent with the above data. These results showed that the antibacterial effect of two single antibacterial methods (PTT or catalytic therapy) was limited, which was not enough to completely kill the bacteria. After the combination of these antibacterial methods, the antibacterial effect of Cu SASs/NPC was significantly enhanced, showing the combined antibacterial effect of PTT-catalytic therapy.

To clarify the antibacterial mechanism of Cu SASs/NPC, the morphological changes of bacteria and the level of ROS closely related to the death of bacteria were further studied. The antibacterial effects of Cu SASs/NPC itself and Cu SASs/NPC + H_2O_2 were mainly to cause the surface collapse of bacteria (Fig. 5a–b), while the photothermal antibacterial performance of Cu SASs/NPC (Cu SASs/NPC + NIR light) was mainly to cause the collapse of bacterial skeleton structure. On the whole, the bacterial morphology damage caused by the combined treatment group (Cu SASs/NPC + H_2O_2 + NIR light) was the most serious, and the antibacterial effect was also the best. In addition, the changes in the ROS content of the two types of bacteria under different treatment conditions were tested. In the groups of (5)–(8), the level of ROS in bacteria increased. Among them, the fluorescence intensity of ROS in group (8) was the strongest. The fluorescence of ROS in synergistic treatment group (8) of Cu SASs/NPC + H_2O_2 + NIR light was strongest, indicating that the peroxidase-like catalytic treatment combined with PTT of Cu SASs/NPC could generate lots of ROS in bacteria (Fig. 5c–d, and Fig. S20). In addition, to verify the loss of membrane integrity, protein leakage tests were carried out on *E. coli* and *MRSA* after different treatments using the BCA protein assay kit (Fig. S21). Cu SASs/NPC incubated with H_2O_2 and under 808 nm laser irradiation showed the highest protein leakage, indicating that the mild photothermal effect together with good ROS generation induced by Cu SASs/NPC promoted the protein leakage of bacteria. On this basis, the possible combined antibacterial mechanism of Cu SASs/NPC was proposed: (1) Cu SASs/NPC can be used as peroxidase-like nanozymes to efficiently produce •OH in presence of H_2O_2, which can cause cell wall damages; (2) the mild photothermal performance can not only kill some bacteria, but also improve the peroxidase-like catalytic activity of Cu SASs/NPC; (3) at mild temperature, the destructive physical interaction of bacteria with sharp edges of Cu SASs/NPC increases due to the increase of component movement; (4) Cu SASs/NPC can also be used as GSH-Px-like nanozymes, which can consume GSH in the internal environment of bacteria, thereby improving the efficacy of catalytic therapy (Fig. S22). Therefore, the antibacterial mechanism of Cu SASs/NPC mainly includes photothermal killing, ROS generation, and GSH consumption (Fig. 5e).

To assess the *in vivo* antibacterial effect of Cu SASs/NPC, the animal model of *MRSA*-infected wounds was constructed (Fig. 6a). Blab/c mice were randomly divided into the following seven groups: (1) control; (2) PBS + NIR light; (3) H_2O_2; (4) Cu SASs/NPC; (5) Cu SASs/NPC + H_2O_2; (6) Cu SASs/NPC + NIR light; (7) Cu SASs/NPC + H_2O_2 + NIR light. The concentrations of Cu SASs/NPC and H_2O_2 are 100 μg/mL and 100 μM, respectively. After different treatments, the wounds were photographed every day, and the changes in wound size and the weight of mice were recorded. The temperature change of the wounds was monitored by an infrared thermal camera. These results exhibited that the wound temperature increased markedly under 808 nm laser irradiation (1.0 W/cm^2, 2 min) in the groups of Cu SASs/NPC + NIR light (6) and Cu SASs/NPC + H_2O_2 + NIR light (7), while in the groups of control and PBS + NIR light, the wound temperature only slightly changed (Fig. 6b, and Fig. S23). The temperature of wounds should be controlled at ~45 °C to demonstrate the combined therapeutic performance of Cu SASs/NPC. After 5 days of treatment, there was no difference in relative wound area in groups of PBS + NIR light (2) and H_2O_2 (3) compared with control group (1). The wound size in the groups of Cu SASs/NPC (4), Cu SASs/NPC + H_2O_2 (5), and Cu SASs/NPC + NIR (6) were significantly smaller than that of the control group (1), indicating that this treatment method can effectively prevent wound infection and promote wound healing. As expected, in the group treated with Cu SASs/NPC + H_2O_2 + NIR (7), the wound healing was the best compared with the other groups (1)–(6) (Fig. 6c, e). Photographs and quantitative analysis of bacterial colonies after 5 days of treatment showed that the amount of bacteria remaining in the groups of Cu SASs/NPC + H_2O_2 (5) and Cu SASs/NPC + NIR (6) was significantly less than that of the control group (1), while the combined treatment group (Cu SASs/NPC + H_2O_2 + NIR light) had the least bacterial residues compared with the control group (1), which also explained the reason for the fastest wound healing in the combined treatment group (Fig. 6d, f). At the end of the treatment, the wound skin of the mice was taken out for hematoxylin and eosin (H&E) staining and Masson staining to further evaluate the wound healing. In the groups of control (1), PBS + NIR light (2), H_2O_2 (3), and Cu SASs/NPC (4), the wound still showed signs of inflammation and skin epidermal disorder. However, the wound had mild inflammation in the groups of Cu SASs/NPC + H_2O_2 (5) and Cu SASs/NPC + NIR (6). More importantly, the Cu SASs/NPC + H_2O_2 + NIR (7) group exhibited no signs of inflammation and formed a complete epidermal layer, showing that the wound had completely healed (Fig. 6g–h). All these results demonstrated Cu SASs/NPC combined with PTT and peroxidase-like catalytic treatment could achieve better bactericidal effects, thereby promoting wound healing.

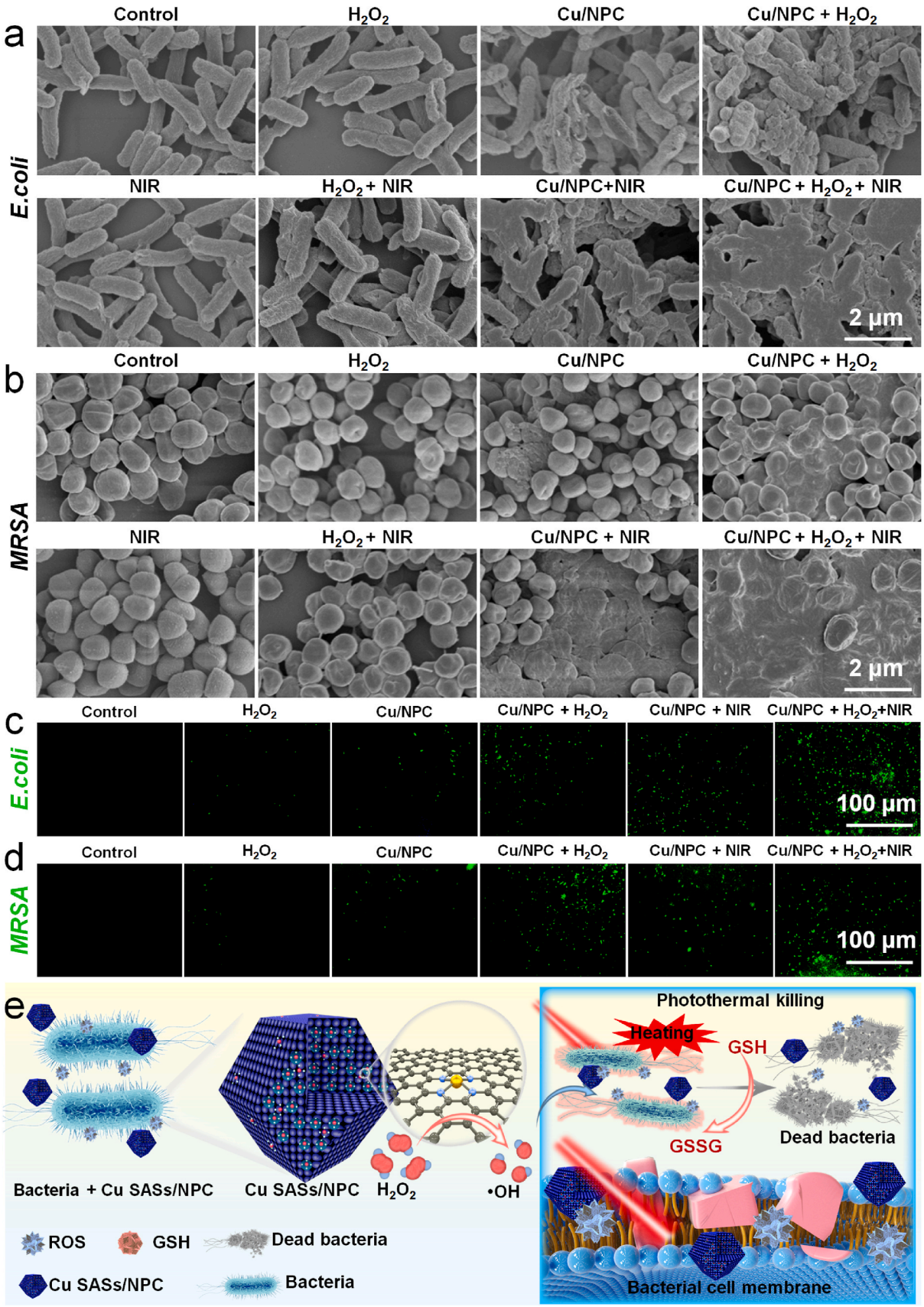

Fig. 5. Antibacterial mechanism of Cu SASs/NPC. SEM images of (a) *E. coli* samples and (b) *MRSA* samples after various treatments (control, NIR light; H_2O_2; NIR light + H_2O_2; Cu SASs/NPC; Cu SASs/NPC + H_2O_2; Cu SASs/NPC + NIR light; Cu SASs/NPC + H_2O_2 + NIR light). Fluorescence staining images of (c) *E. coli* and (d) *MRSA* using DCFH-DA probe after various treatments. (e) Schematic diagram of the antibacterial mechanism of Cu SASs/NPC. The mechanism of antibacterial mainly includes photothermal killing, ROS production, and GSH depletion.

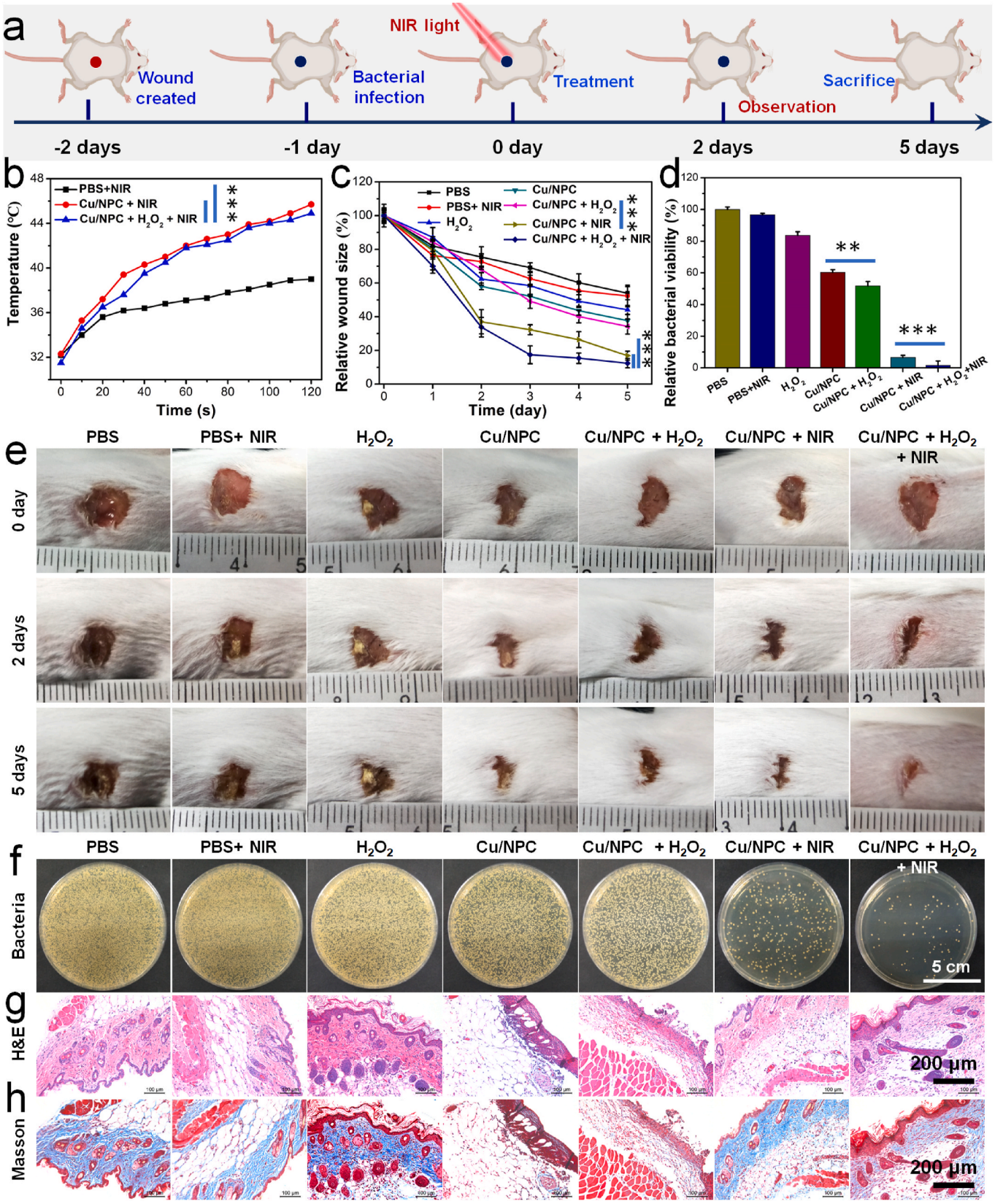

Fig. 6. *In vivo* antibacterial performance of Cu SASs/NPC. (a) *In vivo* antibacterial protocol in mice. (b) Temperature change curves of mice treated with Cu SASs/NPC after 808 nm laser irradiation (1.0 W/cm^2, 2 min). (c) Wound area, and (e) wound photographs of mice after various treatments at different treatment time. (d) Quantitative analysis and (f) photographs of bacterial colonies after 5 days treatment. (g) H&E and (h) Masson staining of the bacteria infected tissues after different treatments. Statistical analysis was performed using the Student's two-tailed *t*-test (***P < 0.001, **P < 0.01, and *P < 0.05).

The cytotoxicity of Cu SASs/NPC was further evaluated using human umbilical vein endothelial cells (HUVECs) (Fig. S24a). It found that the synthesized Cu SASs/NPC showed no obvious cytotoxicity on HUVECs, indicating the good biocompatibility of Cu SASs/NPC. No obvious hemolysis was found even at the high concentration of 100 μg/mL, indicating the excellent blood compatibility of Cu SASs/NPC (Fig. S24b). During the treatment period, the body weight of the mice did not significantly change among the various treatment groups (Fig. S25), indicating that the treatment process did not affect the normal growth of mice [51]. To evaluate the biosafety of Cu SASs/NPC, the main organs (heart, liver, spleen, lung, and kidney) were collected for H&E staining, and the blood were collected for blood routine, and blood biochemical testing after different treatments. There were no significant differences in blood routine and blood biochemical parameters in the co-treatment

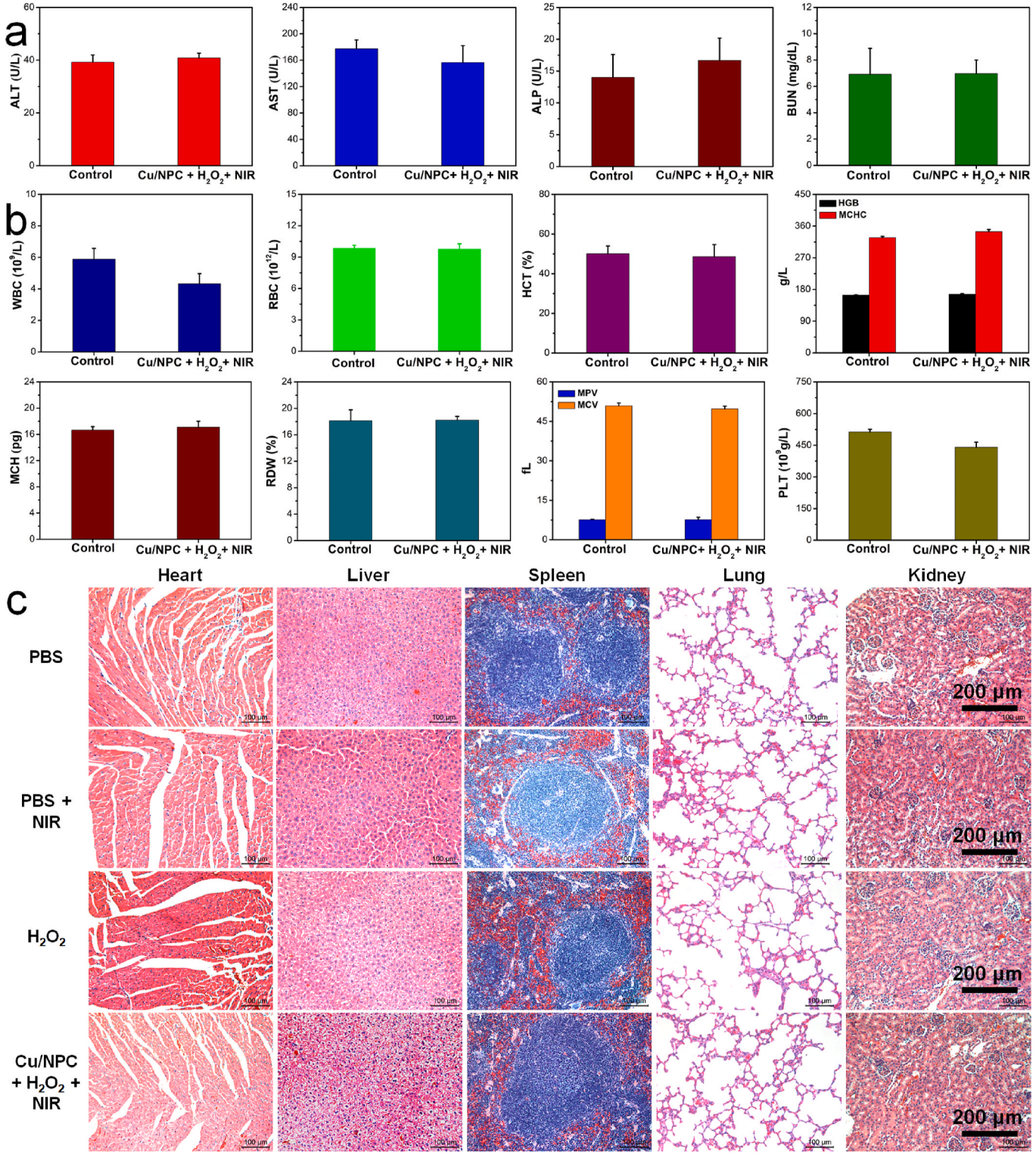

Fig. 7. Biosafety assessment of Cu SASs/NPC. (a) The blood biochemistry, and (b) blood panel analysis test of mice after 5 days of treatment (control, Cu SASs/NPC + H_2O_2 + NIR light). (c) H&E staining images of major organs after different treatments.

group (Cu SASs/NPC + H_2O_2 + NIR light) compared with healthy mice in the control group (1) (Fig. 7a–b). No visible damage, inflammation, or abnormality were observed in the H&E staining of the main organs of the mice, indicating that Cu SASs/NPC had no significant toxicity in the treatment of MRSA-infected wounds in mice (Fig. 7c and Fig. S26). The above results proved that Cu SASs/NPC could be used as safe and excellent antibacterial nanomaterials for photothermal-catalytic antibacterial treatment.

3. Conclusions

In summary, dual peroxidase-like and GSH-like nanozymes of Cu SASs/NPC synthesized through the PEAP strategy were used for photothermal-catalytic antibacterial treatment. The doping of Cu significantly enhanced the peroxidase-like catalytic activity, GSH-depleting function, and photothermal property of Cu SASs/NPC compared with NPC without Cu doping. The obtained Cu SASs/NPC could act as both peroxidase-like and GSH-P_x-like nanozymes, not only can efficiently catalyze H_2O_2 to generate •OH, but also have satisfactory GSH consumption ability, which had an obvious killing effect on two types of bacteria. Moreover, the Cu SASs/NPC had remarkable NIR absorption and could convert NIR light energy into overheating under laser irradiation. The resulting photothermal effect could significantly enhance the peroxidase-like catalytic activity of Cu SASs/NPC, thereby generating more ROS and obtaining better *in vitro* antibacterial performance. More importantly, *in vivo* experiments showed that Cu SASs/NPC effectively destroyed internal bacterial infections propagated at wounds by MRSA pathogens, thereby achieving better wound healing. Collectively, our work highlights the excellent antibacterial effects of Cu SASs/NPC and further expands the bio-applications of Cu-containing SASs.

CRediT authorship contribution statement

Xianwen Wang: conceived and designed the experiments, All authors discussed the results and commented on the manuscript, performed experiments, All authors discussed the results and commented on the manuscript, discussed the results, All authors discussed the results and commented on the manuscript, Writing – original draft, All authors discussed the results and commented on the manuscript. **Qianqian Shi:** performed experiments, All authors discussed the results and commented on the manuscript. **Zhengbao Zha:** discussed the results. **Dongdong Zhu:** performed experiments, All authors discussed the results and commented on the manuscript. **Lirong Zheng:** performed experiments, All authors discussed the results and commented on the manuscript. **Luoxiang Shi:** performed experiments. **Xianwen Wei:** discussed the results, All authors discussed the results and commented on the manuscript. **Lian Lian:** performed experiments, All authors discussed the results and commented on the manuscript. **Konglin Wu:** performed experiments, All authors discussed the results and commented on the manuscript, discussed the results, All authors discussed the results and commented on the manuscript, Writing – original draft, All authors discussed the results and commented on the manuscript. **Liang Cheng:** conceived and designed the experiments, All authors discussed the results and commented on the manuscript, discussed the results, Writing – original draft, All authors discussed the results and commented on the manuscript.

Declaration of competing interest

The authors declare no competing financial interest.

Acknowledgment

This article was partially supported by the National Research Programs of China (2016YFA0201200), the National Natural Science Foundation of China (U20A20254, 52072253), Collaborative Innovation Center of Suzhou Nano Science and Technology, a Jiangsu Social Development Project (BE2019658), a Project Funded by the Priority Academic Program Development (PAPD) of Jiangsu Higher Education Institutions, and the Science and Technology Project Foundation of Suzhou (no. SS202093). The authors also appreciate meaningful suggestions from Prof. Shoujie Liu at Chemistry and Chemical Engineering of Guangdong Laboratory.

Appendix A. Supplementary data

Supplementary data to this article can be found online at https://doi.org/10.1016/j.bioactmat.2021.04.024.

References

[1] H. Koo, R.N. Allan, R.P. Howlin, P. Stoodley, L. Hall-Stoodley, Targeting microbial biofilms: current and prospective therapeutic strategies, Nat. Rev. Microbiol. 15 (12) (2017) 740–755.
[2] L. Wang, X. Zhang, X. Yu, F. Gao, Z. Shen, X. Zhang, S. Ge, J. Liu, Z. Gu, C. Chen, An all-organic semiconductor C_3N_4/PDINH heterostructure with advanced antibacterial photocatalytic therapy activity, Adv. Mater. 31 (33) (2019), 1901965.
[3] X. Zhang, G. Zhang, M. Chai, X. Yao, W. Chen, P.K. Chu, Synergistic antibacterial activity of physical-chemical multi-mechanism by TiO_2 nanorod arrays for safe biofilm eradication on implant, Bioact. Mater. 6 (1) (2021) 12–25.
[4] Z. Song, Y. Wu, Q. Cao, H. Wang, X. Wang, H. Han, pH-responsive, light-triggered on-demand antibiotic release from functional metal-organic framework for bacterial infection combination therapy, Adv. Funct. Mater. 28 (23) (2018), 1800011.
[5] Y. Sang, W. Li, H. Liu, L. Zhang, H. Wang, Z. Liu, J. Ren, X. Qu, Construction of nanozyme-hydrogel for enhanced capture and elimination of bacteria, Adv. Funct. Mater. 29 (22) (2019), 1900518.
[6] F. Cao, L. Zhang, H. Wang, Y. You, Y. Wang, N. Gao, J. Ren, X. Qu, Defect-rich adhesive nanozymes as efficient antibiotics for enhanced bacterial inhibition, Angew. Chem. Int. Ed. 58 (45) (2019) 16236–16242.
[7] F. Wei, X. Cui, Z. Wang, C. Dong, J. Li, X. Han, Recoverable peroxidase-like Fe_3O_4@MoS_2-Ag nanozyme with enhanced antibacterial ability, Chem. Eng. J. 408 (2021), 127240-127240.
[8] E. Zhang, X. Zhao, J. Hu, R. Wang, S. Fu, G. Qin, Antibacterial metals and alloys for potential biomedical implants, Bioact. Mater. 6 (8) (2021) 2569–2612.
[9] J. Xi, G. Wei, L. An, Z. Xu, Z. Xu, L. Fan, L. Gao, Copper/carbon hybrid nanozyme: tuning catalytic activity by the copper state for antibacterial therapy, Nano Lett. 19 (11) (2019) 7645–7654.
[10] B. Huang, L. Tan, X. Liu, J. Li, S. Wu, A facile fabrication of novel stuff with antibacterial property and osteogenic promotion utilizing red phosphorus and near-infrared light, Bioact. Mater. 4 (2019) 17–21.
[11] Y. Zhang, D. Li, J. Tan, Z. Chang, X. Liu, W. Ma, Y. Xu, Near-infrared regulated nanozymatic/photothermal/photodynamic triple-therapy for combating multidrug-resistant bacterial infections via oxygen-vacancy molybdenum trioxide nanodots, Small 17 (1) (2021), 2005739.
[12] L. Yan, J. Mu, P. Ma, Q. Li, P. Yin, X. Liu, Y. Cai, H. Yu, J. Liu, G. Wang, A. Liu, Gold nanoplates with superb photothermal efficiency and peroxidase-like activity for rapid and synergistic antibacterial therapy, Chem. Commun. 57 (9) (2021) 1133–1136.
[13] J. Xi, G. Wei, Q. Wu, Z. Xu, Y. Liu, J. Han, L. Fan, L. Gao, Light-enhanced sponge-like carbon nanozyme used for synergetic antibacterial therapy, Biomater. Sci. 7 (10) (2019) 4131–4141.
[14] Z. Guo, Y. Liu, Y. Zhang, X. Sun, F. Li, T. Bu, Q. Wang, L. Wang, A bifunctional nanoplatform based on copper manganate nanoflakes for bacterial elimination via a catalytic and photothermal synergistic effect, Biomater. Sci. 8 (15) (2020) 4266–4274.
[15] W. Yin, J. Yu, F. Lv, L. Yan, L.R. Zheng, Z. Gu, Y. Zhao, Functionalized nano-MoS_2 with peroxidase catalytic and near-infrared photothermal activities for safe and synergetic wound antibacterial applications, ACS Nano 10 (12) (2016) 11000–11011.
[16] J. Shan, K. Yang, W. Xiu, Q. Qiu, S. Dai, L. Yuwen, L. Weng, Z. Teng, L. Wang, Cu_2MoS_4 nanozyme with NIR-II light enhanced catalytic activity for efficient eradication of multidrug-resistant bacteria, Small 16 (40) (2020), 2001099.
[17] J. Shan, X. Li, K. Yang, W. Xiu, Q. Wen, Y. Zhang, L. Yuwen, L. Weng, Z. Teng, L. Wang, Efficient bacteria killing by Cu_2WS_4 nanocrystals with enzyme-like properties and bacteria-binding ability, ACS Nano 13 (12) (2019) 13797–13808.
[18] Y. Zhang, Y. Pi, Y. Hua, J. Xie, C. Wang, K. Guo, Z. Zhao, Y. Yong, Bacteria responsive polyoxometalates nanocluster strategy to regulate biofilm microenvironments for enhanced synergetic antibiofilm activity and wound healing, Theranostics 10 (22) (2020) 10031–10045.
[19] M. Xu, Y. Hu, Y. Xiao, Y. Zhang, K. Sun, T. Wu, N. Lv, W. Wang, W. Ding, F. Li, B. Qiu, J. Li, Near-infrared-controlled nanoplatform exploiting photothermal promotion of peroxidase-like and OXD-like activities for potent antibacterial and anti-biofilm therapies, ACS Appl. Mater. Interfaces 12 (45) (2020) 50260–50274.
[20] W. Klare, T. Das, A. Ibugo, E. Buckle, M. Manefield, J. Manos, Glutathione-disrupted biofilms of clinical Pseudomonas aeruginosa strains exhibit an enhanced antibiotic effect and a novel biofilm transcriptome, Antimicrob. Agents Chemother. 60 (8) (2016) 4539.

[21] X. Wang, L. Fan, L. Cheng, Y. Sun, X. Wang, X. Zhong, Q. Shi, F. Gong, Y. Yang, Y. Ma, Z. Miao, Z. Zha, Biodegradable nickel disulfide nanozymes with GSH-depleting function for high-efficiency photothermal-catalytic antibacterial therapy, iScience 23 (7) (2020), 101281.

[22] X. Wang, X. Zhong, Z. Zha, G. He, Z. Miao, H. Lei, Q. Luo, R. Zhang, Z. Liu, L. Cheng, Biodegradable CoS_2 nanoclusters for photothermal-enhanced chemodynamic therapy, Appl. Mater. Today 18 (2020), 100464.

[23] Y. Shi, J. Yin, Q. Peng, X. Lv, Q. Li, D. Yang, X. Song, W. Wang, X. Dong, An acidity-responsive polyoxometalate with inflammatory retention for NIR-II photothermal-enhanced chemodynamic antibacterial therapy, Biomater. Sci. 8 (21) (2020) 6093–6099.

[24] Y. Liu, Z. Guo, F. Li, Y. Xiao, Y. Zhang, T. Bu, P. Jia, T. Zhe, L. Wang, Multifunctional magnetic copper ferrite nanoparticles as fenton-like reaction and near-infrared photothermal agents for synergetic antibacterial therapy, ACS Appl. Mater. Interfaces 11 (35) (2019) 31649–31660.

[25] Y. Wu, G. Deng, K. Jiang, H. Wang, Z. Song, H. Han, Photothermally triggered nitric oxide nanogenerator targeting type IV pili for precise therapy of bacterial infections, Biomaterials (2021) 268.

[26] Q. Gao, X. Zhang, W. Yin, D. Ma, C. Xie, L. Zheng, X. Dong, L. Mei, J. Yu, C. Wang, Z. Gu, Y. Zhao, Functionalized MoS_2 nanovehicle with near-infrared laser-mediated nitric oxide release and photothermal activities for advanced bacteria-infected wound therapy, Small 14 (45) (2018), 1802290.

[27] S. Zhang, L. Jin, J. Liu, Y. Liu, T. Zhang, Y. Zhao, N. Yin, R. Niu, X. Li, D. Xue, S. Song, Y. Wang, H. Zhang, Boosting chemodynamic therapy by the synergistic effect of Co-catalyze and photothermal effect triggered by the second near-infrared light, Nano-Micro Lett. 12 (1) (2020) 180.

[28] Z. Tang, P. Zhao, H. Wang, Y. Liu, W. Bu, Biomedicine meets Fenton Chemistry, Chem. Rev. (2021), https://doi.org/10.1021/acs.chemrev.0c00977.

[29] B. Ma, S. Wang, F. Liu, S. Zhang, J. Duan, Z. Li, Y. Kong, Y. Sang, H. Liu, W. Bu, L. Li, Self-assembled copper-amino acid nanoparticles for in situ glutathione "AND" H_2O_2 sequentially triggered chemodynamic therapy, J. Am. Chem. Soc. 141 (2) (2019) 849–857.

[30] L.-S. Lin, T. Huang, J. Song, X.-Y. Ou, Z. Wang, H. Deng, R. Tian, Y. Liu, J.-F. Wang, Y. Liu, G. Yu, Z. Zhou, S. Wang, G. Niu, H.-H. Yang, X. Chen, Synthesis of copper peroxide nanodots for H_2O_2 self-supplying chemodynamic therapy, J. Am. Chem. Soc. 141 (25) (2019) 9937–9945.

[31] X. Wang, X. Zhong, H. Lei, Y. Geng, Q. Zhao, F. Gong, Z. Yang, Z. Dong, Z. Liu, L. Cheng, Hollow Cu_2Se nanozymes for tumor photothermal-catalytic therapy, Chem. Mater. 31 (16) (2019) 6174–6186.

[32] Y. Liu, J. Wu, Y. Jin, W. Zhen, Y. Wang, J. Liu, L. Jin, S. Zhang, Y. Zhao, S. Song, Y. Yang, H. Zhang, Copper(I) phosphide nanocrystals for in situ self-generation magnetic resonance imaging-guided photothermal-enhanced chemodynamic synergetic therapy resisting deep-seated tumor, Adv. Funct. Mater. 29 (50) (2019), 1904678.

[33] H. Xiang, W. Feng, Y. Chen, Single-atom catalysts in catalytic biomedicine, Adv. Mater. 32 (8) (2020), 1905994.

[34] B. Xu, H. Wang, W. Wang, L. Gao, S. Li, X. Pan, H. Wang, H. Yang, X. Meng, Q. Wu, L. Zheng, S. Chen, X. Shi, K. Fan, X. Yan, H. Liu, A single-atom nanozyme for wound disinfection applications, Angew. Chem. Int. Ed. 58 (15) (2019) 4911–4916.

[35] X. Lu, S. Gao, H. Lin, J. Shi, Single-atom catalysts for nanocatalytic tumor therapy, Small (2021), 2004467.

[36] J. Pei, R. Zhao, X. Mu, J. Wang, C. Liu, X.-D. Zhang, Single-atom nanozymes for biological applications, Biomater. Sci. 8 (23) (2020) 6428–6441.

[37] X. Lu, S. Gao, H. Lin, L. Yu, Y. Han, P. Zhu, W. Bao, H. Yao, Y. Chen, J. Shi, Bioinspired copper single-atom catalysts for tumor parallel catalytic therapy, Adv. Mater. 32 (36) (2020), 2002246.

[38] M. Huo, L. Wang, Y. Wang, Y. Chen, J. Shi, Nanocatalytic tumor therapy by single-atom catalysts, ACS Nano 13 (2) (2019) 2643–2653.

[39] M. Huo, L. Wang, H. Zhang, L. Zhang, Y. Chen, J. Shi, Construction of single-iron-atom nanocatalysts for highly efficient catalytic antibiotics, Small 15 (31) (2019), 1901834.

[40] K. Wu, X. Chen, S. Liu, Y. Pan, W.-C. Cheong, W. Zhu, X. Cao, R. Shen, W. Chen, J. Luo, W. Yan, L. Zheng, Z. Chen, D. Wang, Q. Peng, C. Chen, Y. Li, Porphyrin-like Fe-N_4 sites with sulfur adjustment on hierarchical porous carbon for different rate-determining steps in oxygen reduction reaction, Nano Res 11 (12) (2018) 6260–6269.

[41] P. Yin, T. Yao, Y. Wu, L. Zheng, Y. Lin, W. Liu, H. Ju, J. Zhu, X. Hong, Z. Deng, G. Zhou, S. Wei, Y. Li, Single cobalt atoms with precise N-coordination as superior oxygen reduction reaction catalysts, Angew. Chem. Int. Ed. 55 (36) (2016) 10800–10805.

[42] L. Huang, J. Chen, L. Gan, J. Wang, S. Dong, Single-atom nanozymes, Sci. Adv. 5 (5) (2019) eaav5490.

[43] K. Wu, K. Sun, S. Liu, W.C. Cheong, Z. Chen, C. Zhang, Y. Pan, Y. Cheng, Z. Zhuang, X. Wei, Y. Wang, L. Zheng, Q. Zhang, D. Wang, Q. Peng, C. Chen, Y. Li, Atomically dispersed Ni-Ru-P interface sites for high-efficiency pH-universal electrocatalysis of hydrogen evolution, Nano Energy 80 (2021), 105467.

[44] K. Wu, F. Zhan, R. Tu, W.-C. Cheong, Y. Cheng, L. Zheng, W. Yan, Q. Zhang, Z. Chen, C. Chen, Dopamine polymer derived isolated single-atom site metals/N-doped porous carbon for benzene oxidation, Chem. Commun. 56 (63) (2020) 8916–8919.

[45] Y. Pan, Y. Chen, K. Wu, Z. Chen, S. Liu, X. Cao, W.-C. Cheong, T. Meng, J. Luo, L. Zheng, C. Liu, D. Wang, Q. Peng, J. Li, C. Chen, Regulating the coordination structure of single-atom Fe-N_xC_y catalytic sites for benzene oxidation, Nat. Commun. 10 (1) (2019) 4290.

[46] H. Shang, X. Zhou, J. Dong, A. Li, X. Zhao, Q. Liu, Y. Lin, J. Pei, Z. Li, Z. Jiang, D. Zhou, L. Zheng, Y. Wang, J. Zhou, Z. Yang, R. Cao, R. Sarangi, T. Sun, X. Yang, X. Zheng, W. Yan, Z. Zhuang, J. Li, W. Chen, D. Wang, J. Zhang, Y. Li, Engineering unsymmetrically coordinated Cu-S_1N_3 single atom aites with enhanced oxygen reduction activity, Nat. Commun. 11 (1) (2020) 3049.

[47] M. Zhao, N. Zhang, R. Yang, D. Chen, Y. Zhao, Which is better for nanomedicines: nanocatalysts or single-atom catalysts? Adv. Healthcare Mater. (2020), 2001897.

[48] X. Wang, X. Wang, X. Zhong, G. Li, Z. Yang, Y. Gong, Z. Liu, L. Cheng, V-TiO_2 nanospindles with regulating tumor microenvironment performance for enhanced sonodynamic cancer therapy, Appl. Phys. Rev. 7 (4) (2020), 041411.

[49] R. Hu, Y. Fang, M. Huo, H. Yao, C. Wang, Y. Chen, R. Wu, Ultrasmall $Cu_{2-x}S$ nanodots as photothermal-enhanced Fenton nanocatalysts for synergistic tumor therapy at NIR-II biowindow, Biomaterials 206 (2019) 101–114.

[50] A. Li, X. Li, X. Yu, W. Li, R. Zhao, X. An, D. Cui, X. Chen, W. Li, Synergistic thermoradiotherapy based on PEGylated Cu_3BiS_3 ternary semiconductor nanorods with strong absorption in the second near-infrared window, Biomaterials 112 (2017) 164–175.

[51] J. Chi, X. Zhang, C. Chen, C. Shao, Y. Zhao, Y. Wang, Antibacterial and angiogenic chitosan microneedle array patch for promoting wound healing, Bioact. Mater. 5 (2) (2020) 253–259.